CHAPTER 14

Laser Ablation Electrospray Ionization Mass Spectrometry: Mechanisms, Configurations and Imaging Applications

PETER NEMES* AND AKOS VERTES*

Department of Chemistry, W. M. Keck Institute for Proteomics Technology and Applications, The George Washington University, Washington, DC, USA
*Email: vertes@gwu.edu; petern@gwu.edu

14.1 Introduction

In recent years, the combination of midinfrared (mid-IR) laser ablation sampling with efficient ionization methods for direct analysis by mass spectrometry (MS) has been successfully implemented in a growing number of ambient ionization techniques.[1–3] The primary driving force behind this approach is to combine the microsampling capabilities of focused laser beams with the high ion yields achievable by electrospray and photoionization sources. Laser-ablation sampling at 2.94 μm wavelength is especially advantageous in biomedical analysis, where the native water content of the sample acts as a matrix due to the strong absorption by the OH stretching mode. Since the first implementation of a mid-IR laser-ablation electrospray ionization (LAESI) source,[4] several closely related techniques have followed,[5–9] and the corresponding literature has expanded to include numerous journal publications (see Table 14.1) and three book chapters.[10–12]

New Developments in Mass Spectrometry No. 2
Ambient Ionization Mass Spectrometry
Edited by Marek Domin and Robert Cody

Published by the Royal Society of Chemistry, www.rsc.org

Table 14.1 Milestones in LAESI development and applications.

Operation modality	Geometry	Figures of Merits	Specimen	Detected Compounds	Ref.
In situ/ in vivo	Conventional	Quantitation (4 orders of magnitude); LOD = 8 fmol, up to 66.5 kDa; *in vivo* analysis	Urine; whole blood; plant organs (*T. patula*)	Drug standards, lipids, metabolites, proteins	4
		Reactive LAESI for structural elucidation	*M. musculus* brain	Metabolites, lipids	24
		Animal tissue, *in vitro*	*T. californica* electric organ	Metabolites	23
		Soft ion generation	Chemical standards	Thermometer ions	37
	Heat-assisted	Polar–apolar compounds; quantitation (3 orders of magnitude)	Avocado mesocarp and *M. musculus* sections	Metabolites, lipids	57
Biomarker discovery	Conventional	Human cell lines transfected with Human T-lymphotropic virus type 1	T lymphocyte cells (CEM and H9), kidney epithelial cells (293T)	Metabolites, lipids, proteins	25
		Oncovirus-infected cell lines	B lymphocytes infected with Kaposi's sarcoma-associated herpesvirus (KSHV)	Metabolites, lipids, proteins	27
		~600 cyanobacterial cells	*Anabaena sp.* PCC7120	Metabolites, proteins	26
	Plume collimation	Small cell populations: 6 cells; quantitation (6 orders of magnitude); LOD = 600 amol	Cheek cells (human), rat insulinoma β-cells (RIN5mF), sea urchin eggs	Metabolites, drug standards	22
	Fiber optic	Single cells	*A. cepa*, *N. pseudonarcissus*, *L. pictus*	Metabolites	18–20
	Fiber optic	Subcellular organelles	*A. cepa*	Metabolites	21,22
		50 μm depth resolution	*S. lynise* leaf	Metabolites, ink dyes	13
Depth profiling	Conventional	350 μm lateral	*S. lynise* and *A. squarrosa* leaves;	Metabolites (primary, secondary)	10,13,15
2D MSI	Conventional	250 μm lateral	*R. norvegicus* section	Metabolites, osmolites, lipids	10,15,16
	Fiber optic	Cell-by-cell imaging	*A. cepa*	Sugars, polysaccharides, metabolites	17
3D MSI	Conventional	350 μm lateral by 50 μm depth resolution	*A. squarrosa*	Metabolites	10,14,15

Despite the growing number of analytical applications of LAESI MS in tissue imaging,[13–17] single-cell analysis[18–22] and metabolomics,[11,14,16,18,21–27] the understanding of mechanisms underlying the LAESI process is incomplete. There are four major factors that contribute to ion production in LAESI. In the sampling step, mid-IR laser ablation of the water-containing target takes place, resulting in an expanding plume of vapor and fine particulates representing the sample. Simultaneously, an electrospray is produced that generates a charged dynamic droplet plume that travels toward the mass spectrometer.[28] The third process takes place in the region where the laser-ablation plume merges with the electrospray. In this phase, the particulates from the sample coalesce with the charged droplets from the electrospray. This is followed by ion production that unfolds similarly to the conventional electrospray process, except that in LAESI the charged droplets are seeded with the ablated sample particles. As this last step has been extensively discussed in the literature, in the second segment of this chapter we focus our attention on the three first steps, laser ablation, electrospray formation and coalescence in the merging plumes. Each of these processes is complex in itself, and understanding their combination is essential to gain an insight into the mechanisms of LAESI.

In order to improve the efficiency of the individual processes, various LAESI configurations have been developed. Two of these variants of the technique rely on changes in the delivery of the laser energy (optical fiber-based focusing and ablation in transmission geometry), one interferes with the plume dynamics (plume collimation), and another facilitates droplet desolvation (heat-assisted LAESI). In the third segment of this chapter we explore how these altered modalities perform compared to the conventional LAESI source, and what additional information they provide on the mechanistic steps.

In the final segment of the chapter we describe the different approaches pursued in molecular imaging applications. We demonstrate the advantages of MS imaging (MSI) with LAESI under ambient conditions. Combining lateral imaging and depth profiling, enables three-dimensional imaging on rectangular grids. We show the utility of ion-mobility separation (IMS) in reducing chemical interferences in MSI of complex samples. To retain more of the biological information in MSI of tissues, cell coordinates are extracted from microscope images for a cell-by-cell imaging strategy.

14.2 Sampling and Ionization Mechanisms

14.2.1 Midinfrared Laser Ablation of Biomedical Samples

LAESI measurements capitalize on atmospheric-pressure (AP) ablation of the specimen of interest. The experimental setup for a traditional LAESI system is depicted in Figure 14.1(A). Instructions on assembling the setup and developing measurement methods have been provided elsewhere.[10,15] Sampling is initiated by focusing a midinfrared (mid-IR) laser beam of

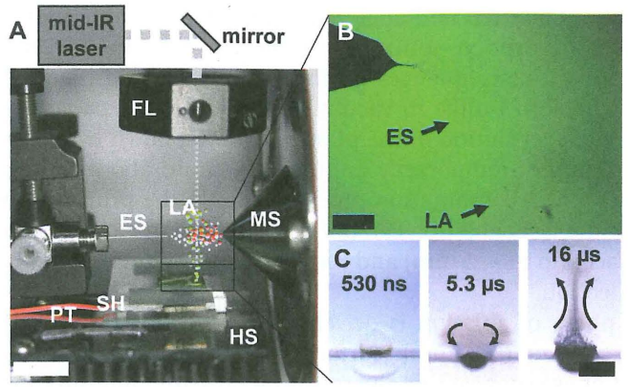

Figure 14.1 Schematic of laser-ablation electrospray ionization (LAESI) and relevant processes. (A) Resonant excitation of water by a midinfrared laser beam (dashed lines) ablates the sample. The generated plume (LA, *green dots*) is intercepted by charged droplets from an electrospray (ES, *grey dots*). Ions produced from charged droplets seeded by sample molecules (*red dots*) are analyzed by a mass spectrometer (MS). The sample holder (SH) is equipped with Peltier stage (PT) for cooling and a heat sink (HS). Scale bar = 25 mm. (B) Fast imaging captures interception of LA particles by ES plume. Scale bar = 100 µm. (C) Steps of LA include a hemispherical plume produced by phase explosion (left panel), collapse of the primary ablation plume (shown at 5.3 µs in the middle), and ejection of particulate matter (shown at 16 µs in the right panel). Scale bar = 1 mm.
(Parts of this figure were adapted from ref. 4 and 30 with permission.)

2.94 µm wavelength and 1–100 ns duration to the surface of the sample.[4] This wavelength is strategically selected because it allows for efficient coupling of the light energy into the specimen material through the adjacent absorption maximum related to the symmetric stretching mode of OH in water that is natively present or added to the sample. As the temperature rises water exhibits nonlinear absorption behavior and becomes increasingly transparent.[29] At sufficiently high fluences, usually at 0.1–5 J cm^{-2} for tissues of high water content, this sudden deposition of energy causes ablation of the sample (Figures 14.1(B) and (C)) on a microscopic scale.

The mechanistic details of mid-IR ablation of water and water-containing biological tissues can be discussed based on results from fast-imaging experiments.[30] Ablation of water occurs through three partially overlapping phases at AP (Figure 14.1(C)). During the first ~100 ns, fast surface evaporation takes place that creates hemispherical vapor plume that exhibits relatively slow expansion.[31] When the temperature in the irradiated surface layer reaches $\sim 0.9T_c$, where T_c is the critical temperature of water, phase explosion occurs that generates a rapidly expanding dense plume of mostly neutral nanosized droplets and particles.[32] This primary ablation plume also contains a small portion of ions, with a yield inferred to be below ~0.01%,[33]

that are directly collected and analyzed in another technique, AP IR matrix-assisted laser desorption ionization (MALDI).[34,35] The AP environment imparts important consequences on the dynamics of the plume created by the phase explosion. Unlike in vacuum, where plume expansion continues indefinitely, at AP evolution of the plume is slowed down by the presence of the background gas, temporarily halting it ~1 mm above the sample surface. Due to rapid recombination processes at AP, the primary ions directly generated by the laser ablation can only be collected in close proximity of the sample surface (up to ~2 mm) and require a high voltage for extraction and efficient collection.[36]

The next phase of ablation is driven by the recoil pressure of the phase explosion exerted on the sample surface. Shock-wave velocity measurements in the liquid phase suggest that the resulting pressure buildup can reach 500 to 900 MPa that relaxes through the expulsion of sample material in the next ~500 μs (Figure 14.1(C)).[30] The momentum carries the droplets and particles of this secondary ablation plume to several millimeters above the sample surface (Figure 14.1(C)). Systematic studies employing fast-imaging experiments, and chemical analysis of the secondary ablation plume suggested that ejected particles of ~5 μm average diameter travel as far as 45 mm above the sample surface before being stopped by the drag force.[36,37] Although this process casts sample material to large distances, the secondary ablation plume lacks the ions necessary for MS analysis.

14.2.2 Electrosprays for Ionization in LAESI

In LAESI, material in the secondary ablation plume is intercepted by an electrospray and ionized to enable mass spectrometric determination of its chemical composition. Fine charged droplets (less than ~5 μm in diameter) are generated by supplying a suitable spray solution (*e.g.*, acidified or basified 50% methanol) through an electrified capillary (*e.g.*, metal or fused silica) (Figure 14.1). Operating parameters of the electrospray such as solution composition, supply rate, and voltage are judiciously chosen to produce a stable spray, preferably in the pulsating or cone-jet regime[28] (Figure 14.1(B)) to continuously supply small droplets for efficient LAESI MS.[4] Incorrectly chosen operating parameters result in spraying modes with low ion yields (dripping and burst regimes)[38,39] or low stability (a stable regime).[40] Nonaxial spraying regimes (rim emission) are detrimental to the LAESI signal as the density of the droplets close to the spray axis is low and the droplet velocities point away from the mass-spectrometer inlet. The pulsating regime provides relatively high ion yields with current oscillations in the 1 to 7 kHz range.[38,41] These pulsation frequencies provide a sufficiently high duty cycle, so the temporal overlap between the laser-ablation plume and the electrospray is acceptable. Although the ion yield with the pulsating regime does not reach the values seen for the cone jet regime, it is substantially easier to establish and maintain without spray-current monitoring.[38]

14.2.3 Merging Ablation Plume and Electrospray

Control experiments confirmed that normal operating conditions in LAESI do not generate ions by corona discharge at the emitter, *i.e.* ionization by an electrospray is pivotal. The electrospray plume, with its axis typically 15 to 30 mm above the sample surface, intercepts the secondary laser-ablation plume, thus promoting coalescence between the ablated particulate matter and the electrospray droplets, seeding the latter with molecules of the sample.

Phase Doppler anemometry measurements indicate that methanol–water mixtures electrosprayed in the pulsating regime, produce droplets of 2 to 10 μm in diameter with 0.5 to 5 m s^{-1} velocities gradually slowing as they move away from the emitter.[28,42,43] Fast-imaging experiments of water ablation by an Er:YAG laser at 2.94 μm wavelength and 5.4 J cm^{-2} fluence indicate that the initial velocity of the ejected material at the sample surface, v_0, is 150 m s^{-1}.[30] As the ablation plume rises, the particle velocity diminishes due to the drag force in the ambient environment. Assuming that Stokes law holds for the drag force, the stopping distance for these particles can be expressed as:

$$x_{stop} = 2\rho R^2 v_0 / 9\mu \tag{14.1}$$

where ρ is the density of the sample, R is the radius of the particle, and μ is the dynamic viscosity of air.[37] Substituting a 15 mm and 30 mm stopping distances, 150 m s^{-1} initial velocity, and room-temperature material properties for the environment, particle diameters of 5.7 μm and 8.1 μm are obtained. This means that the laser-ablated particles, which slow down close to stopping at the axis of the electrospray, have diameters similar to those of the charged droplets. Indeed, slow ablated particles are desired as in typical LAESI configurations they travel perpendicular to the trajectories of the charged droplets. By reducing the particle velocities close to zero, they can be entrained by the velocity field induced by the electrospray droplets and move together with them.

Several models exist to describe the scavenging of microscopic aerosol particles by small charged raindrops[44,45] but their validity is limited to situations when the droplet diameter is at least ten times larger than that of the particle. Under these circumstances the trajectory of the droplet is not affected by a collision with the particle. Collisions are also facilitated by the attractive polarization forces induced by the charged droplets.[46] Another consequence of the large size difference is that every collision leads to particle capture by the droplet.

As the particle and droplet sizes in LAESI are similar to each other, the collision efficiencies and coalescence efficiencies can be significantly different. The governing parameter in these collisions is the Weber number, a relative measure of inertia and surface tension, $We = p_1(v_L - v_S)^2 D_s/\sigma_1$, where D_S is the diameter of the smaller colliding partner, v_L and v_S are the velocities of the larger and the smaller colliding partners, and ρ_l and σ_l are the density and the surface tension of the liquid, respectively. Depending on the value of

the Weber number, the collision events follow different scenarios.[47] For We < 2, there is no coalescence, as the collision results in either bouncing or grazing. For $2 <$ We < 5, the outcome of the collision depends on the impact parameter. For small impact parameters, coalescence occurs but for large impact parameter values after transient fusing separation takes place. In the $5 <$ We < 7 range, the coalescence efficiency is close to one, whereas at higher We values, $7 <$ We, it gradually declines to zero. Thus, as long as the relative velocity of the particle and the droplet are in a range that results in $5 <$ We < 7, the coalescence is very efficient.

The resulting seeded droplets are entrained by fluid dynamic and electrostatic forces into the mass spectrometer through the orifice of a sampling cone located ~10 mm away from the electrospray emitter tip (Figures 14.1 and 14.2). Throughout this process, ions are produced by the solvated ion evaporation[48] or the charge residue mechanism.[49] The chemical composition of generated gas-phase ions is determined by the mass spectrometer.

14.2.4 Ion Internal Energies and Conformations

Based on accumulated evidence, the LAESI ionization is efficient and nondestructive to most biomolecules. The ion yield has been found to be ~10–100-fold higher than in typical AP IR-MALDI.[36] This is because ~99.99% of the ablation plume is in the form of neutrals that are efficiently ionized by the electrospray. Early observations indicated that LAESI was capable of producing intact ions from molecules as large as human serum albumin with a molecular mass of 66 556 Da.[4] The presence of multiply charged ions in LAESI mass spectra of proteins and peptides supported the notion of mechanistic similarity with electrospray ionization.

To gauge the internal energy of ions generated by LAESI, survival yields of benzyl-substituted benzylpyridinium thermometer ions were measured using solution and tissue samples.[37] The results showed that the ions generated by LAESI and electrospray had indistinguishable internal energies. Furthermore, LAESI mass spectra of labile biomolecules, such as peptides and vitamin B_{12}, showed no signs of fragmentation. In contrast, MALDI mass spectra of the latter from 2,5-dihydroxybenzoic acid (DHB) matrix exhibited two major fragment ions. Similarly to LAESI, low internal energies are observed in other ambient ionization sources utilizing electrosprays, including desorption electrospray ionization (DESI), electrosonic spray ionization, and paper spray ionization.[50,51] A qualitative explanation of the observation that the mid-IR laser ablation in LAESI does not increase the internal energy of the ions relies on a mechanistic argument. As the ionized neutrals are mostly produced by the recoil pressure-induced material ejection, the produced particulates are dislodged by a pressure pulse and are not heated significantly by the laser. Therefore, the ions generated from the ejected particulates only reflect the internal energy contributed by the electrospray process.

Another property associated with the internal energy of ions is their conformations. Higher internal energy makes more extreme conformations accessible for the ion. To assess the conformation of LAESI-generated ions, mobility measurements were performed in a traveling-wave IMS system on protein standards, cell pellets and tissue samples.[52,53] Using multiply charged myoglobin ions for calibration,[54] the collision cross sections of lysozyme and ubiquitin ions are found to be within 4% of the values established by electrospray ionization.[55] Such close similarity in collision cross section is an indication of analogous conformations of ions produced by LAESI and electrospray.

14.3 LAESI Geometries and Configurations

Because ionization is decoupled both spatially and temporally from ablation sampling, LAESI has been afforded various configurations with many having spawned specific applications. In the original reflection arrangement (Figure 14.2), the focused laser beam impinging on the sample surface and the ensuing ablation plume sampled by the electrospray are on the same side of the sample (front side). In the less-explored inverted geometry (Figure 14.3), the back side of the sample is illuminated and the ablation plume evolving on the front side is intercepted by the electrospray (transmission geometry). Although these configurations share analogy with those developed for MALDI,[56] the relative positions of various components (*e.g.*, the electrospray source and inlet orifice of the mass spectrometer) enable additional variants in LAESI. The selected configurations influence the interception efficiency between the laser-ablation plume and electrospray, thus affecting the ion signal intensities.

Both of these basic LAESI geometries give rise to additional variants based on the relative configuration of specific components. Examples of the reflection geometry include the conventional, heat-assisted, and fiber-optic arrangements, as presented in Figure 14.2. Likewise, the transmission geometry has found applications in conventional and fiber-optic (plume collimation) arrangements (Figure 14.3). The different configurations support specific application niches. A brief summary of developmental milestones and applications is reviewed in Table 14.1. Below, the fundamental considerations and leading performance metrics are described for the various arrangements.

14.3.1 Conventional LAESI in Reflection Geometry

The original or *conventional* LAESI system developed in 2007 demonstrated broad utility in the direct analysis of biological fluids, tissues and cells. The experimental setup, depicted in Figure 14.1, utilized reflection geometry (see left panel of Figure 14.2(A)). A laser beam of 2.94 μm wavelength was generated by an Er:YAG laser with less than 100-ns pulse length and steered using gold-coated mirrors through a calcium fluoride (CaF_2) lens to yield

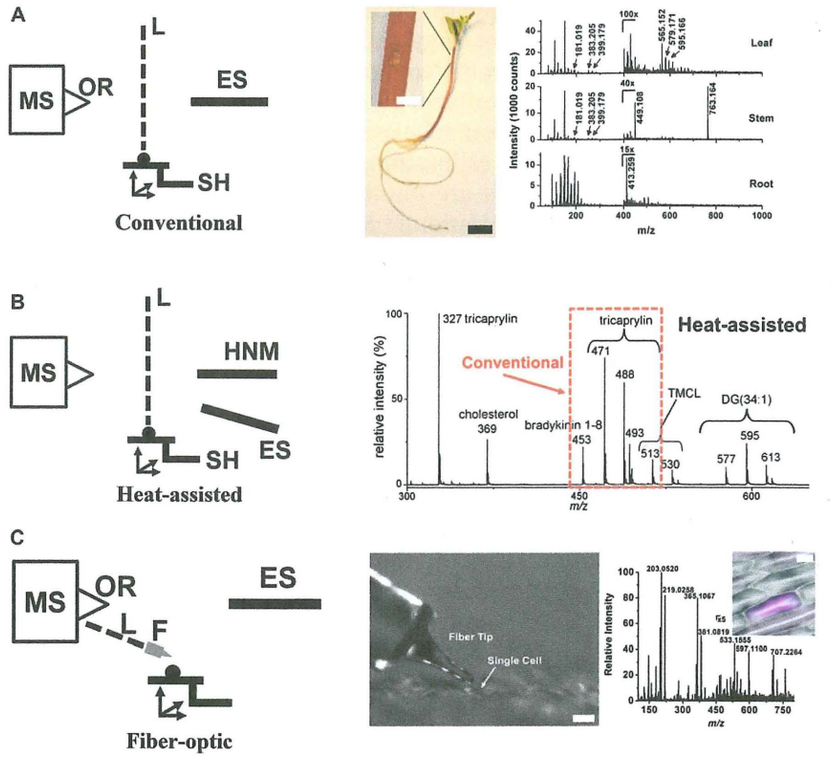

Figure 14.2 Reflection geometry LAESI in representative configurations. (A) Conventionally, the laser beam (L) is focused using lenses or mirrors to enable *in situ* and *in vivo* sampling. Root, stem, and leaf organs of a live plant were profiled with ~250 μm resolution. Scale bars = 10 mm (black), 1 mm (white). (B) In heat-assisted LAESI, adding a gas jet heated by a microchip (HNM) extends the detectable compound types to less-polar molecules. The ions detected by conventional LAESI are in the red rectangle. (C) In fiber-LAESI, a sharpened optical fiber (F) produced significantly smaller ablation areas. By holding the fiber tip 30 μm above the specimen surface, single epidermal cells were ablated with 50 μm resolution. Scale bar = 100 μm. Key: mass spectrometer (MS), MS sampling cone orifice (OR), sample holder (SH) and electrospray (ES).
(Parts of this figure were adapted from ref. 4, 18 and 57 with permission.)

circular ablation craters of ~350–400 μm diameter. As shown in the right panel of Figure 14.2(A), these ablation dimensions proved sufficiently small to profile various organs of a French marigold seedling (*Tagetes patula*) without compromising its viability. The leaf, stem and root were measured *in vivo*, revealing organ-specific chemical composition. Apart from small analysis areas, rapid operation was equally important to enable deciphering the undisturbed metabolic composition of the specimen. The time

requirement of the analysis was less than ~1 s/sample, enabling the study of metabolic changes that occur on the time scale of seconds or slower. As a consequence, conventional LAESI can be used to take a snapshot of the chemical composition of biological systems or follow temporal changes on a timescale of seconds and longer.

Analysis by LAESI is chemically specific and quantitative. Detected ions range from singly charged small compounds (drugs, metabolites, lipids, *etc.*) to multiply charged species (midsized proteins) (see Table 14.1). The high-mass capabilities were demonstrated for 66.5 kDa human serum albumin detected with a charge state distribution between ~39 and ~52 protons in the mass spectra. The LAESI MS signal was quantitative for solutions of drug standards for over 4 orders of magnitude in concentration. For conventional LAESI, the lower limit of detection was 8 fmol.[4] These figures of merit have recently been extended by plume collimation and a high-performance mass spectrometer to 6 orders of magnitude dynamic range and 600 amol limit of detection.[22]

In the years following the original design, technological advances were pivotal to achieving improved analytical performance in conventional LAESI. Short laser pulses (5–10 ns full width at half-maximum) based on a Nd:YAG laser-driven optical parametric oscillator (OPO), high repetition rates (up to 100 Hz), and laser pulse energy stability (< 7% variation) promoted improved signal-to-noise ratios and analytical reproducibility. A planoconvex ZnSe lens or a reflective microscope objective (50105-02, Newport, Irvine, CA) ensured improved focusing of the incident mid-IR beam, yielding circular sampling spots with diameters reduced to ~100 μm.

As smaller ablation spots, required for improved local analysis, contain less material for detection, the efficiency of ionization has to be improved. A systematic study found that LAESI ion yield increased with a decreasing flow rate of the electrospray solution (see Figure 9.3(b) in Reference 10). For example, a change from 300 nL min^{-1} to ~50 nL min^{-1} resulted in a ~10-fold improvement in signal intensity.

In turn, higher ion yields facilitated measurements on various animal tissues, making, *e.g.*, the detection of 200–300 endogenous metabolites possible in rat brain tissue sections.[16] To avoid the evaporative loss of water and chemical degradation in these samples, a Peltier cooling element was incorporated into the sample holder that kept the sample frozen during analyses (Figure 14.1). Likewise, control of the ambient temperature and humidity *via* an enclosure prevented condensation of water on the cooled sample surfaces (*e.g.*, frozen brain tissue section). As a result, LAESI MS has evolved to achieve nontargeted analysis of multiple compounds in diverse samples types (see Table 14.1).

14.3.2 Heat-assisted LAESI

The conventional setup has recently been modified to enhance the ionization of less polar species. Maintaining the reflection geometry, the

electrospray plume was intercepted at a 20–30° angle by a jet of nitrogen gas (180–360 mL min^{-1}) heated to ~170–220 °C using a microchip.[57] Schematics of this heat-assisted setup are shown in the left panel of Figure 14.2(B). A systematic study found the ionization efficiency to increase with gas temperature and flow rate for compounds of low polarity (*e.g.*, estrone), whereas ionization of polar species (*e.g.*, bradykinin 1-8) appeared independent of these experimental variables. Heat-assisted LAESI successfully ionized a number of apolar specimens that were not detected using conventional LAESI, including polyaromatic hydrocarbons (*e.g.*, perylene and naphtho[2,3-α]pyrene) and neutral lipids (cholecalciferol, cholesterol, DG(34:1), and tricaprylin) (see right panel of Figure 14.2(B)). This LAESI modality was also quantitative, spanning over a 3 orders of magnitude concentration range.

Complementary performance by heat-assisted LAESI proved particularly useful for the interrogation of complex biological samples. Measurements on avocado (*Persea americana*) mesocarp, mouse brain, and pansy (*Viola*) petals yielded mass spectra enhanced for compounds of low polarity. Polar lipids such as phospholipids and monogalactosyl diglycerides gave generally strong response with conventional LAESI, whereas detection of apolar lipids such as triglycerides and cholesterol benefited from the heated gas stream.

14.3.3 Microsampling using Fiber Optics

Further development of LAESI to enable microsampling of specimens required changes in laser pulse delivery. Due to the limitations of coherent mid-IR sources, primarily the large beam divergence (*e.g.*, 5 to 10 mrad for OPOs) and spherical aberrations associated with conventional methods of focusing based on lenses and mirrors, the produced spot diameters are many times larger (~100 to 200 μm) than the diffraction-limited value (~1.5 μm). To alleviate these difficulties, the sharpened end of an optical fiber can be used to deliver laser light to much smaller spots. In this arrangement, similar to scanning near-field optical microscopy, the illuminated area is determined by the sharpness of the tip, not by the diffraction limit defined by the wavelength of the light. Although the spot sizes used in fiber-based LAESI (~30 μm) are still significantly above the diffraction limit, they are much smaller than in the case of conventional focusing. Schematics of the setup are shown in Figure 14.2(C).

A typical setup used a germanium oxide-based (GeO_2) fiber (outlet) whose end was etched to create a tip with a radius of curvature, $R = \sim 15$ μm, following protocols discussed elsewhere.[20] The tip was positioned $\sim 2R$ distance at ~45° incidence angle from the specimen surface. Mid-IR light of appropriate energy (*e.g.*, <600 μJ) and repetition rate (*e.g.*, 100 Hz) was coupled through the inlet. As a result, the material was ablated from under the tip across a circular area of $\sim 2.5R$ average diameter, usually within 1 s or 100 laser pulses.[18] Ablation craters on thin plan tissues usually measured 30–40 μm in diameter, affording an opportunity to access the chemical

composition of area- or volume-limited samples such as single cells under ambient conditions.

Ablation of single cells followed a remarkable mechanism. Unlike free solutions ablated in the conventional setup (on a sample holder such as a glass slide), plant cells have rigid walls that act as a natural boundaries, confining the ablation in space. Time-lapse imaging and study of the LAESI signal revealed that at least 2 consecutive laser pulses delivered 10–100 ms apart were necessary to rupture the cell wall, thus providing access to the intracellular content.[19] Ejection or evaporation of the cytosol completed the process, beyond which no mass spectrometric signal was detected.

Interrogations requiring single-cell resolution have particularly benefited from fiber-optic LAESI. Representative examples include metabolic analysis of onion (*Allium cepa*) and daffodil (*Narcissus pseudonarcissus*) single plant cells as well as individual eggs of sea urchin (*Lytechinus pictus*) with ~25–50 μm probe diameters. More than 300 different ions were registered below *m/z* 800 with acceptable signal-to-noise ratios. Of the detected ions, 35 were assigned to primary (*e.g.*, oligosaccharides) and secondary metabolites (*e.g.*, glycosidic flavonoids).[18] Furthermore, analysis at single-cell resolution permitted profiling cells of different pigmentation as well as age, and finding differences in metabolic composition (*e.g.*, arginine *vs.* alliin concentrations). Likewise, the small analysis area made chemical differentiation of oil gland and neighboring cells possible in leaves of bitter orange (*Citrus aurantium*).[17]

When combined with advanced protocols in sample preparation, *e.g.*, microdissection, fiber optics in LAESI has also opened the door to subcellular investigations. In a recent example, microsurgical needles of approximately 1 μm tip diameter helped to cut away the cell wall, exposing the cytoplasm and organelles of single cells.[21] Because the sharpened tip of the optical fiber was dimensionally comparable to the nucleus, this LAESI modality was able to attain the cell compartment-specific chemistries *in situ*. Nuclear and cytoplasmic small metabolites were differentiated with a multivariate data interpretation tool, orthogonal projections to latent structures discriminant analysis (OPLS-DA). The results showed higher abundance for the hexose and alliin in the cytoplasm and arginine and glutamine in the nucleus. By extension, increasingly sophisticated microdissection can help to extend subcellular analysis to progressively smaller cells and subcellular organelles, or other volume-limited samples.

14.3.4 LAESI in Transmission Geometry

In transmission geometry, a thin sample, *e.g.*, tissue section, is illuminated by the laser beam from the back side, and the ablation plume develops on the front side. The advantage of this approach is that the electrospray that intercepts the ablation plume and the focusing lens are on different sides of the sample (see the left panel in Figure 14.3(A)). Thus, high-performance, short working distance, lenses can be used to achieve ablation with

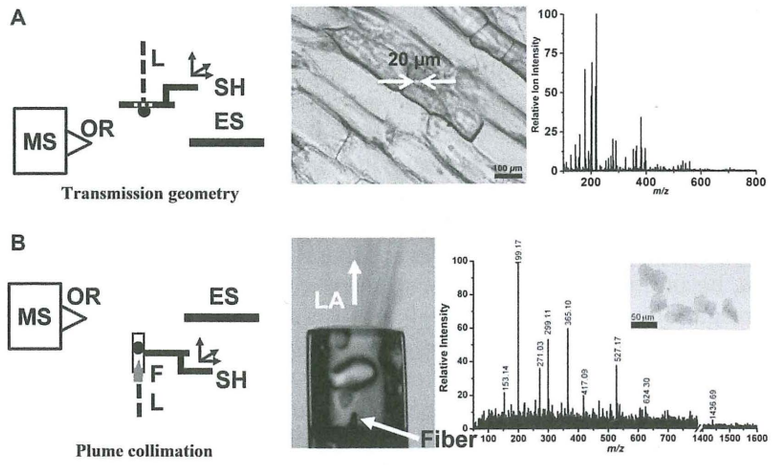

Figure 14.3 Transmission geometry LAESI with representative configurations. The laser beam (L) was focused on the back side of the sample in the transmission geometry, allowing (A) to ablate thin specimens (*e.g.*, dried residues, tissue sections, and single cells). (B) Confinement of the ablation plume (LA) in a capillary enhances the interaction with the electrospray for more efficient ionization. The sharpened optical fiber (F) is visible in the capillary. Primary metabolites were measured for 6 cheek cells (inset). Key: mass spectrometer (MS), MS sampling cone orifice (OR), sample holder (SH), and electrospray (ES). (Parts of this figure were adapted from ref. 22 with permission.)

significantly reduced spot sizes. For example, using a short working distance aspherical lens (BD-2, Thorlabs, Newton, NJ), 20 µm ablation spot and LAESI signal were achieved on a monolayer of *A. cepa* epidermal cells (see the right panel in Figure 14.3(A)).[58] This arrangement also enables the *in situ* monitoring of the sample during ablation by a long distance microscope from the front side. In a proof-of-principle application, transmission geometry LAESI was used to compare the flavonoids in the tulip leaf and bulb epidermis.[59]

14.3.5 Plume Collimation

In this variant of the transmission geometry arrangement, the sample was ablated under spatial confinement. The specimen was loaded into a fused silica capillary, and a sharpened optical fiber was inserted coaxially through the back end of the capillary to achieve ablation.[22] A systematic study of this configuration using a high-performance mass spectrometer found that the analytical figures of merit were significantly better than those reported for the conventional LAESI. The 600 amol limit of detection and the 6 orders of magnitude dynamic range for quantitation achieved by plume collimation compared favorably to the 8 fmol and 4 orders of magnitude values established for conventional LAESI, respectively.[4]

These improvements were ascribed to fundamental differences in the dynamics of the ablation plume as well as a higher ion collection and transfer efficiency associated with the high-resolution mass spectrometer. Unlike during the laser pulse exposure of a free-standing specimen, such as a droplet or liquid film, ablation of a sample in an enclosure results in the confinement of the generated plume. Results inferred from optical imaging of the ablation plume corroborate this point. In conventional LAESI, significant radial expansion of the plume is observed (see Figure 14.1(B)), whereas in the case of plume collimation by confinement in a capillary the divergence of the ablation plume is significantly reduced (see right panel in Figure 14.3(B)). Thus, a greater portion of the ejected material reaches the electrospray plume resulting in a stronger signal.

The lower limit of detection and wider dynamic range with plume collimation extended ambient MS to smaller amounts and higher complexity of samples. For example, less than 100 rat insulinoma β-cells (RIN5mF) with an average diameter of 10 µm were successfully analyzed, yielding significant ion intensities for 35 different ions (primary metabolites and lipids). The studied cell populations were progressively reduced for larger cell types: mass spectra of 20 megakaryoblast cells (50 µm diameter), six cheek cells (30–50 µm diameter) (see right panel in Figure 14.3(B)), and a single sea urchin egg (~100 µm diameter) were measured using plume collimation.

14.4 Spatial Profiling and Imaging Applications

14.4.1 Lateral Molecular Imaging

Local analysis in conventional LAESI enabled MS imaging (MSI) under ambient conditions. In this modality, the chemical composition of the tissue is determined pixel by pixel according to the workflow shown in Figure 14.4(A). The tissue section is mounted on a sample holder in the focal plane of the mid-IR laser beam (Figure 14.1) and translated in two dimensions (X and Y) using a computer-controlled two-axis translation stage, while the location (X–Y coordinates of the pixel) and the corresponding LAESI mass spectra are coregistered. A distribution of a chemical species in the interrogated area can be reconstructed into a false-color image by selecting the corresponding ion and plotting its signal intensities against pixel locations.

Successful LAESI MSI requires the consideration of various experimental factors. Imaging in two dimensions calls for pixel-by-pixel ablation over the domains of interest and the entire depth of the tissue section. Reducing the imaging time requirement is important to improve the throughput, and minimize the data file size to facilitate subsequent data analysis. The time allocated for two-dimensional (2D) MSI, $t_{\mathrm{MSI,2D}}$, is given by:

$$t_{\mathrm{MSI,2D}} = \frac{d_x}{R_x}\frac{d_y}{R_y}\left(t_{\mathrm{dwell}} + t_{\mathrm{pos}}\right) \tag{14.2}$$

where a rectangular area of the sample with d_x and d_y dimensions is interrogated at R_x and R_y step sizes in the X and Y dimensions, respectively, t_{dwell} is the time of analysis at each pixel (dwell time), and t_{pos} is the average time required to translate between consecutive pixels/rows. The dwell time is judiciously determined prior to an imaging experiment by considering specimen thickness, repetition rate of the laser, and the material removal rate by the focused beam, with the latter mainly dependent on laser fluence and the tensile strength of the sample. For soft tissues of plants and animals of 50–500 μm thickness, dwell times of 1–5 s/pixel were successful under ~1 J cm^{-2} radiant exposes.[13,15,16] At 10 Hz laser pulse repetition rate and 1 s spectrum integration time, the mass spectrometric signal was found to decay in less than 3 s, permitting to complete imaging of a 12.5×10.5 mm^2 sample at 200 μm resolution in ~3 h.

On plant and animal tissue sections, conventional 2D LAESI MSI provided molecular distributions for various polar compounds, including primary and secondary metabolites, lipids, and proteins. Imaging of frozen rat brain sections (Figure 14.4(B)) by conventional LAESI coupled to a high mass-resolution mass spectrometer deciphered different distribution patterns for the isobars γ-aminobutyric acid (GABA) and choline (Figure 14.4(B)). To help discover the colocalization of selected ions, Pearson crosscorrelation analysis was implemented.[16] In one example, the cholesterol and PC(O-33:3) and/or PE(O-36:3) plasmalogens were observed to colocalize in the corpus callosum of the brain. Unlike tissues of animal origin, plant tissue surfaces are directly amenable to imaging because their waxy cuticle acts as a natural barrier to dehydration rendering freezing of the specimen unnecessary during MSI. For example, the variegated leaves of the zebra plant contained high amounts of methoxykaempferol glucoronide in the yellow sectors, whereas the kaempferol-(diacetylcoumaryl-rhamnoside) was distributed evenly across the yellow and green areas (Figure 14.4(B)).[13] These examples illustrate that 2D LAESI MSI can determine the distribution of diverse compound types in tissues without requiring special treatment.

More recently, the heat-assisted LAESI configuration has also been implemented in MSI. The imaging protocol was identical to conventional LAESI. Molecular images determined for polar anthocyanins showed good agreement with results obtained by the conventional approach (Figure 14.4(D)), with the added potential to extend MSI to apolar compounds.[57] The performance metrics for conventional and heat-assisted LAESI imaging are comparable to other ambient MSI techniques, such as DESI, AP MALDI, surface desorption AP chemical ionization, and probe electrospray ionization.[1,3]

14.4.2 Depth Profiling

Tissue ablation by consecutive laser pulses at the same location results in the deepening of the crater and serves as the basis of molecular depth profiling. Scanning electron microscopy (SEM) and Z-stack imaging by optical

microscopy indicated that a single laser pulse of ~2 J cm^{-2} fluence impinging on the upper surface (adaxial) of a leaf ablated the waxy cuticle and portions of the epidermal and palisade cell layers.[13] The SEM image of the ablation mark is shown in Figure 14.5(A) (inset). The cylindrical voxel assigned to the crater measured ~350 μm in diameter and ~50 μm in height corresponding to ~2 nL in volume.[13] In control experiments consecutive laser pulses of 0.2 J cm^{-2} in fluence were delivered to a peace lily leaf whose lower (abaxial) surface had been marked with rhodamine 6G dye. By reducing the pulse-to-pulse variation of the laser energy to less than 7% (*e.g.*, by attenuation *via* a neutral density filter or a Brewster-angle attenuator), a ~50-μm average depth resolution was achieved for routine profiling.[13]

LAESI MS analysis provided depth-resolved metabolite profiles in plant leaves. The first layer, the top ~50 μm, exhibited abundant signal for hexose and disaccharide ions as well as kaempferol or cyanidin glucoside rhamnoside.[13] The latter results agreed with the known accumulation of glycosides in the epidermal layer of leaves to protect the underlying tissue from ultraviolet radiation. In a separate study, the mesophyll layer, between ~50 and 100 μm from the top surface, revealed various ions derived from chlorophyll *a*.[14] Chlorophyll is known to localize in the chloroplasts concentrated in chlorenchyma cells of the mesophyll layer, supporting the findings from LAESI depth profiling.

14.4.3 Imaging in Three Dimensions

The *in situ* combination of 2D LAESI MSI with depth profiling enabled three-dimensional (3D) reconstruction of molecular distributions. In this modality, the depth profile is determined voxel by voxel (Z coordinate) for each X–Y position until a preselected area is rastered. The alternative approach to *in situ* 3D MSI by LAESI would be to perform multiple 2D MSI experiments using only one laser pulse for a given layer. This method, however, is inferior due to positioning errors in returning to a desired pixel for consecutive imaging layers as well as potential drying/contamination of the tissue layer that is exposed to the environment. The imaging resolution is dependent on the same factors that underpin 2D imaging and depth profiling in LAESI: tight focusing of the laser beam (*e.g.*, using reflective microscope objectives), appropriate laser energy with high pulse-to-pulse stability, and accurate positioning elements are needed for a reliable performance. The duration of a 3D MSI experiment, $t_{MSI,3D}$, can be estimated based on:

$$t_{MSI,3D} = \frac{d_x}{R_x}\frac{d_y}{R_y}\frac{d_z}{R_z}\left(t_{dwell} + t_{pos}\right) \tag{14.3}$$

where a volume of d_z thickness is depth-profiled with R_z resolution, and other variables are the same as in eqn (14.2). Similar to lateral imaging, 3D MSI by LAESI requires that ions generated during the ablation of

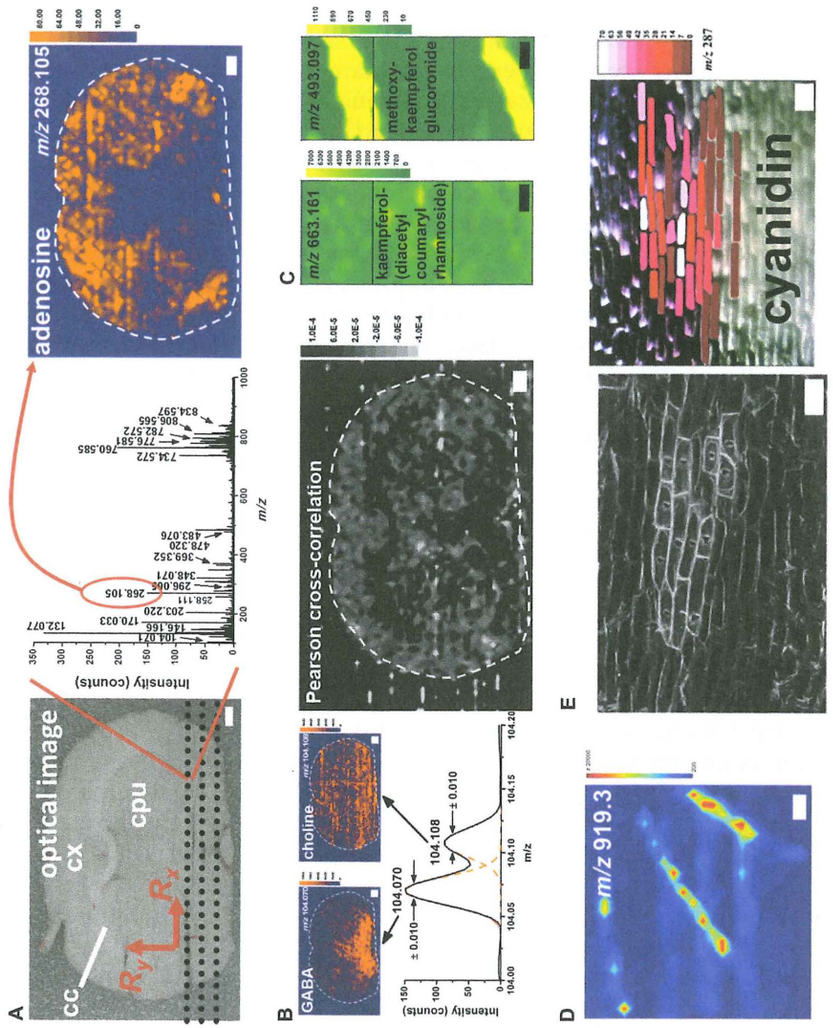

individual voxels be distinguished upon detection. For a mass spectrometer operating at 1 s spectrum integration time, a 0.2 Hz laser repetition rate offers a compromise between lateral/depth resolution and the total time required for imaging, $t_{MSI,3D}$, permitting to explore a $12.5 \times 10.5 \times 0.45$ mm^3 volume with ~350 μm lateral ($R_x = R_y$) and ~40 μm depth resolutions in ~5 h.[14]

3D LAESI MSI has uncovered complex distributions for endogenous metabolites in plant tissue.[14] For example, the molecular ion of cyanidin/kaempferol rhamnoside glucoside was detected only in the top 40 μm of peace lily leaf (Figure 14.5(B)). Flavonoids such as kaempferol glycosides often populate in the upper epidermal layers, presumably to protect the underlying tissue from UV-A and UV-B radiation.[60] Particularly diverse distributions were noted in the variegated leaf of the zebra plant. Acacetin accumulated in the yellow sectors of the leaf in the second and third layers but was present homogeneously in others (Figure 14.5(C)). Kaempferol-(diacetyl coumarylrhamnoside) exhibited elevated levels with homogeneous distributions in the third and fourth layers (Figure 14.5(D)).

Alternative 3D volume reconstruction methods for *in situ* MSI rely on computational assembly of 2D images obtained on serial tissue sections. The procedure originally applied for vacuum MALDI MS images[61] has recently been extended to DESI imaging in the ambient environment.[62] Cryogenic microtomes provide high depth resolution (typically 0.5 to 100 μm) for 3D volume reconstruction, making the technique reproducible, albeit demanding on user experience and analytical throughput. In contrast, 3D LAESI MSI, based on depth profiling, eliminates the need for multiple sectioning of the tissue but the depth resolution, *e.g.*, ~30 μm, is limited

Figure 14.4 Molecular imaging in 2D by LAESI. (A) Imaging workflow: a LAESI mass spectrum is registered for each pixel of a selected area (left panel, rat brain section shown). The false-color image of an ion (*e.g.*, *m/z* 268.105 for adenosine, right panel) is constructed from the spectra (middle panel) by plotting the ion signal intensity against the pixel coordinates. (B) High mass-resolution imaging by conventional LAESI differentiates the distributions of isobars γ-aminobutyric acid (GABA) and choline in rat brain (left panel). Pearson crosscorrelation analysis shows the colocalization of cholesterol, and PC(O-33:3) and/or PE(O-36:3) plasmalogens (right panel). (C) In the variegated leaves of the zebra plant, the kaempferol-(diacetyl coumaryl-rhamnoside) distributes homogeneously in the sample (left panel), whereas methoxykaempferol glucoronide accumulates in the yellow sectors (right panel). (D) Heat-assisted LAESI is used to image the *m/z* 919.3 ion, putatively identified as delphinidin-3-p-coumaroylrhamnosyl-glucoside-5-glucoside, in pansy (*Viola*) petals. (E) Single-cell analysis and cell-by-cell imaging in a heterogeneous cell population by fiber-LAESI (left panel) shows the accumulation of cyanidin in the pigmented cells (right panel). Key: cc, corpus callosum; cx, cerebral cortex; cpu, caudate putamen. For A to D the scale bars = 1 mm, and for E the scale bar = 200 μm.
(Parts of this figure were adapted from ref. 1, 13, 16, 17, 19 and 57 with permissions.)

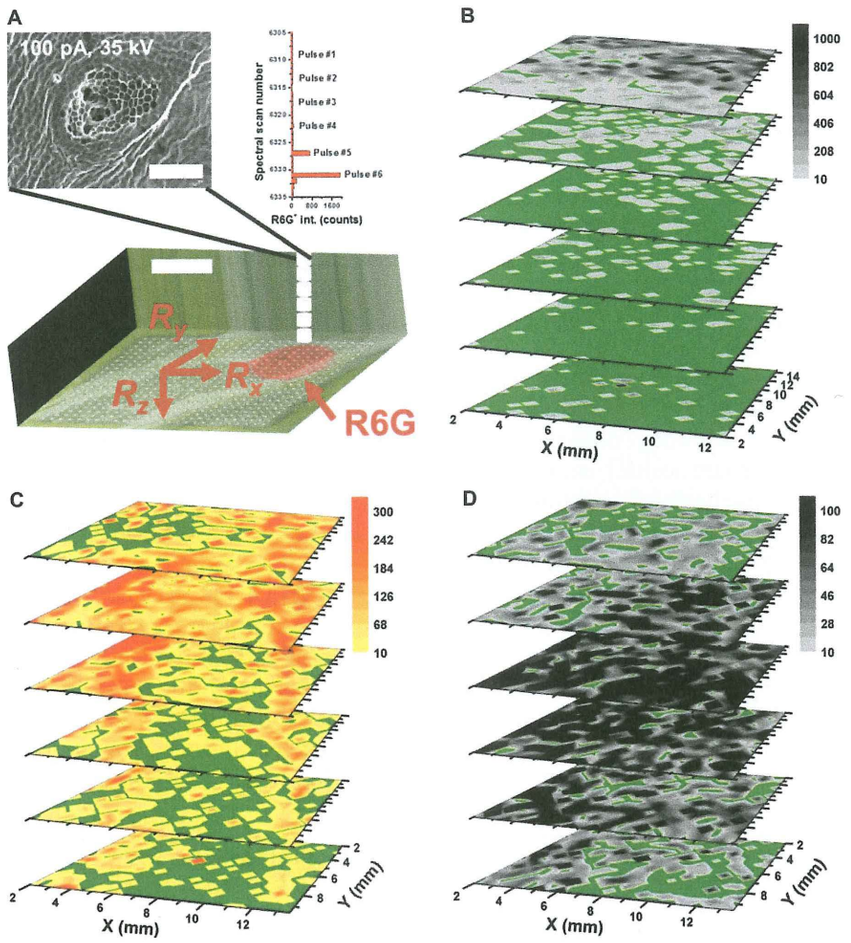

Figure 14.5 Depth profiling and ambient molecular imaging in three dimensions by LAESI. (A) Ablation of a peace lily leaf by consecutive single laser pulses enables depth profiling by LAESI with ~50 μm depth resolution. (B) A combination of depth profiling and 2D MSI results in *in situ* 3D imaging. The epidermal and palisade mesophyll layers of peace lily leaves (*S. lynise*) indicated high abundances of cyanidin/kaempferol rhamnoside glucoside. (C) In the variegated leaves of the zebra plant (*A. squarrosa*), acacetin accumulates in the yellow sectors in the second and third layers, whereas it shows homogeneous distributions in the others. (D) The mesophyll layers are rich in kaempferol-(diacetyl coumarylrhamnoside).
(Parts of this figure were adapted from ref. 1 and 14 with permissions.)

by the tissue removal depth achieved by a single laser pulse. Further improvement of this technique requires enhanced depth-resolution capabilities.

14.5 Cell-by-cell Imaging

The common approach to MSI is to lay a rectangular grid over the tissue surface and collect mass spectra in the grid points. The concern with this method is that the focal spot of the laser in a grid point, *i.e.* a pixel in the image, might overlap with several cells resulting in spectra that reflect the composition of potentially different cells. To overcome this difficulty we introduced the concept of cell-by-cell imaging, where the sampling points are allocated to the centroids of individual cells, thereby assigning the related spectral information as the natural pixels of the image. The obvious advantage of this approach is the greater correlation between cellular composition and pixels in the image.

The tighter focusing and smaller ablation dimensions produced by fiber optics opened the door to imaging with single-cell resolution. As shown in Figure 14.4(E), epidermal cells of *A. cepa* were ablated one cell at a time using a manually positioned, sharpened optical fiber.[19] Multivariate analysis of LAESI mass spectra collected for 36 neighboring cells indicated characteristic differences among the adjacent cells. Cyanidin was detected in significantly higher signal intensity in the pigmented cells, whereas sucrose was uniformly distributed in the cell population.[17]

Manual positioning of the cells for ablation renders this technique slow and cumbersome. To overcome these deficiencies, an automated version has recently been introduced based on object recognition in microscope images of the tissue.[63] Through image-processing algorithms, individual cells were recognized and the coordinates of the corresponding centroids were calculated. This dataset was used to drive the motorized translation stage and bring the cells one-by-one under the tip of the optical fiber for laser ablation. This approach enabled the automated collection of LAESI spectra for cell-by-cell imaging or the selective analysis of a particular cell type based on its morphology, *e.g.*, guard cells in a leaf epidermis. As in the resulting molecular images chemical information from adjacent cells is not mingled, this method can be used to explore cell-to-cell transport and signaling processes.

14.6 Conclusions

The development of LEASI instrumentation and methodology, described in this chapter, has reached the point when the focus is shifting to the ever-growing array of applications. Based on the demonstrated ability of this technique to rapidly identify a wide array of metabolites and lipids in tissues and cells, numerous applications are expected in nontargeted metabolomics and lipidomics. The method is also ripe for comparative studies and biomarker discovery in health, disease and treatment. LAESI has the demonstrated ability to follow biochemical transformations in cells and tissues induced by viral (*e.g.*, Kaposi's sarcoma-associated herpesvirus and human T-lymphotropic virus type 1 and type 3) and bacterial infection. At this point, the coverage for proteins is insufficient for large-scale proteomics, but

selected proteins with elevated local concentrations can be discovered and compared by LAESI MS. Examples include the determination of the subunit composition of phycobilisomal antenna proteins in cyanobacteria, and the discovery of gender-specific protein composition in the gill glands of certain fish.

In conventional LAESI MS experiments, typically ~300 different ions are detected. This number can be indicative of the metabolite and lipid coverage of the LAESI technique. However, significant improvement is demonstrated, with over 1100 different ions detected, when IMS is performed before MS. The introduction of IMS helps to differentiate isobaric species, structural isomers, and different conformations of the same molecule. Further improvement in molecular coverage is expected by combining IMS with reactive LAESI, a technique based on introducing reactants in the electrospray that can enhance the ionization and/or the fragmentation of otherwise non-responsive chemical species.

An important attribute of LAESI MS is its high-throughput capability. Typical measurements of unprocessed samples take on the order of a few seconds. The elimination of sample preparation and lengthy separation steps for metabolomics combined with the reduced analysis time can radically accelerate measurements in this developing field. This is further supported by the recently introduced commercialized version of the LAESI system (DP-1000, Protea Biosciences, Morgantown, WV). With automated sample handling, this instrument offers dramatically improved throughput for metabolomics, reaching hundreds of samples per hour. Commercial availability of the LAESI source will have an increasing impact on the number and variety of applications for this emerging technique.

Acknowledgements

Support is gratefully acknowledged from the U.S. Department of Energy, Office of Basic Energy Sciences, Chemical Sciences, Geosciences, and Biosciences Division under Award DE-FG02-01ER15129 and from the U.S. National Science Foundation under Grant no. CHE-1152302 to AV, and from the US Medical Countermeasure Initiative under Award MCM2J277MW to PN.

References

1. P. Nemes and A. Vertes, *TrAC, Trends Anal. Chem.*, 2012, **34**, 22–34.
2. M. E. Monge, G. A. Harris, P. Dwivedi and F. M. Fernandez, *Chem. Rev.*, 2013, **113**, 2269–2308.
3. C. Wu, A. L. Dill, L. S. Eberlin, G. Cooks and D. R. Ifa, *Mass Spectrom. Rev.*, 2013, **32**, 218–243.
4. P. Nemes and A. Vertes, *Anal. Chem.*, 2007, **79**, 8098–8106.
5. Y. H. Rezenom, J. Dong and K. K. Murray, *Analyst*, 2008, **133**, 226–232.
6. J. S. Sampson, K. K. Murray and D. C. Muddiman, *J. Am. Soc. Mass. Spectrom.*, 2009, **20**, 667–673.

7. I. X. Peng, R. R. O. Loo, E. Margalith, M. W. Little and J. A. Loo, *Analyst*, 2010, **135**, 767–772.
8. G. A. Harris, S. Graf, R. Knochenmuss and F. M. Fernandez, *Analyst*, 2012, **137**, 3039–3044.
9. G. Robichaud, J. A. Barry, K. P. Garrard and D. C. Muddiman, *J. Am. Soc. Mass. Spectrom.*, 2013, **24**, 92–100.
10. P. Nemes and A. Vertes, in *Mass Spectrometry Imaging: Principles and Protocols*, ed. S. S. Rubakhin and J. V. Sweedler, Springer, Berlin, 2010, pp. 159–171.
11. A. Vertes, B. Shrestha and P. Nemes, in *Methodologies for Metabolomics: Experimental Strategies and Techniques*, ed. N. W. Lutz, J. V. Sweedler and R. A. Wevers, Cambridge University Press, Cambridge, 2013, pp. 140–158.
12. B. Shrestha and A. Vertes, in *Plant Metabolism*, ed. G. Sriram, Springer, Berlin, 2014, pp. 31–39.
13. P. Nemes, A. A. Barton, Y. Li and A. Vertes, *Anal. Chem.*, 2008, **80**, 4575–4582.
14. P. Nemes, A. A. Barton and A. Vertes, *Anal. Chem.*, 2009, **81**, 6668–6675.
15. P. Nemes and A. Vertes, *J. Visualized Exp.*, 2010, **43**, e2097.
16. P. Nemes, A. S. Woods and A. Vertes, *Anal. Chem.*, 2010, **82**, 982–988.
17. B. Shrestha, J. M. Patt and A. Vertes, *Anal. Chem.*, 2011, **83**, 2947–2955.
18. B. Shrestha and A. Vertes, *Anal. Chem.*, 2009, **81**, 8265–8271.
19. B. Shrestha, P. Nemes and A. Vertes, *Appl. Phys. A*, 2010, **101**, 121–126.
20. B. Shrestha and A. Vertes, *J. Visualized Exp.*, 2010, **43**, e2144.
21. J. A. Stolee, B. Shrestha, G. Mengistu and A. Vertes, *Angew. Chem., Int. Ed.*, 2012, **51**, 10386–10389.
22. J. A. Stolee and A. Vertes, *Anal. Chem.*, 2013, **85**, 3592–3598.
23. P. Sripadi, J. Nazarian, Y. Hathout, E. P. Hoffman and A. Vertes, *Metabolomics*, 2009, **5**, 263–276.
24. B. Shrestha, P. Nemes, J. Nazarian, Y. Hathout, E. P. Hoffman and A. Vertes, *Analyst*, 2010, **135**, 751–758.
25. P. Sripadi, B. Shrestha, R. L. Easley, L. Carpio, K. Kehn-Hall, S. Chevalier, R. Mahieux, F. Kashanchi and A. Vertes, *PLoS One*, 2010, **5**, e12590.
26. G. Parsiegla, B. Shrestha, F. Carriere and A. Vertes, *Anal. Chem.*, 2012, **84**, 34–38.
27. B. Shrestha, P. Sripadi, C. M. Walsh, T. T. Razunguzwa, M. J. Powell, K. Kehn-Hall, F. Kashanchi and A. Vertes, *Chem. Commun.*, 2012, **48**, 3700–3702.
28. P. Nemes, I. Marginean and A. Vertes, *Anal. Chem.*, 2007, **79**, 3105–3116.
29. R. K. Shori, A. A. Walston, O. M. Stafsudd, D. Fried and J. T. Walsh, *IEEE J. Sel. Top. Quantum Electron.*, 2001, 7, 959–970.
30. I. Apitz and A. Vogel, *Appl. Phys. A*, 2005, **81**, 329–338.
31. Z. Chen, A. Bogaerts and A. Vertes, *Appl. Phys. Lett.*, 2006, **89**, 041503.
32. Z. Y. Chen and A. Vertes, *Phys. Rev. E*, 2008, 77, 036316.

33. C. D. Mowry and M. V. Johnston, *Rapid Commun. Mass Spectrom.*, 1993, 7, 569–575.
34. P. V. Tan, N. I. Taranenko, V. V. Laiko, M. A. Yakshin, C. R. Prasad and V. M. Doroshenko, *J. Mass Spectrom.*, 2004, **39**, 913–921.
35. Y. Li, B. Shrestha and A. Vertes, *Anal. Chem.*, 2007, **79**, 523–532.
36. A. Vertes, P. Nemes, B. Shrestha, A. A. Barton, Z. Y. Chen and Y. Li, *Appl. Phys. A*, 2008, **93**, 885–891.
37. P. Nemes, H. H. Huang and A. Vertes, *Phys. Chem. Chem. Phys.*, 2012, **14**, 2501–2507.
38. L. Parvin, M. C. Galicia, J. M. Gauntt, L. M. Carney, A. B. Nguyen, E. Park, L. Heffernan and A. Vertes, *Anal. Chem.*, 2005, 77, 3908–3915.
39. I. Marginean, P. Nemes and A. Vertes, *Phys. Rev. Lett.*, 2006, **97**, 064502.
40. I. Marginean, P. Nemes and A. Vertes, *Phys. Rev. E*, 2007, **76**, 026320.
41. I. Marginean, L. Parvin, L. Heffernan and A. Vertes, *Anal. Chem.*, 2004, **76**, 4202–4207.
42. Z. Olumee, J. H. Callahan and A. Vertes, *J. Phys. Chem. A*, 1998, **102**, 9154–9160.
43. Z. Olumee, J. H. Callahan and A. Vertes, *Anal. Chem.*, 1999, **71**, 4111–4113.
44. S. N. Grover and K. V. Beard, *J. Atmos. Sci.*, 1975, **32**, 2156–2165.
45. K. V. Beard and S. N. Grover, *J. Atmos. Sci.*, 1974, **31**, 543–550.
46. B. A. Tinsley, R. P. Rohrbaugh, M. Hei and K. V. Beard, *J. Atmos. Sci.*, 2000, **57**, 2118–2134.
47. N. Ashgriz and P. Givi, *Int. Commun. Heat Mass Transfer*, 1989, **16**, 11–20.
48. V. Znamenskiy, I. Marginean and A. Vertes, *J. Phys. Chem. A*, 2003, **107**, 7406–7412.
49. J. F. de la Mora, *Anal. Chim. Acta*, 2000, **406**, 93–104.
50. M. Nefliu, J. N. Smith, A. Venter and R. G. Cooks, *J. Am. Soc. Mass. Spectrom.*, 2008, **19**, 420–427.
51. H. Wang, J. J. Liu, R. G. Cooks and Z. Ouyang, *Angew. Chem., Int. Ed.*, 2010, **49**, 877–880.
52. B. Shrestha and A. Vertes, Proceedings of the 61st ASMS Conference on Mass Spectrometry and Allied Topics, Minneapolis, MN, 2013.
53. B. Shrestha and A. Vertes, *Anal. Chem.*, 2014, **86**, 4308–4315.
54. B. T. Ruotolo, J. L. P. Benesch, A. M. Sandercock, S.-J. Hyung and C. V. Robinson, *Nat. Protoc.*, 2008, **3**, 1139–1152.
55. Clemmer Group Cross Section Database, http://www.indiana.edu/~clemmer/Research/Cross%20Section%20Database/cs_database.php, Last accessed: 12/12/2013.
56. K. Dreisewerd, *Chem. Rev.*, 2003, **103**, 395–425.
57. A. Vaikkinen, B. Shrestha, J. Nazarian, R. Kostiainen, A. Vertes and T. J. Kauppila, *Anal. Chem.*, 2013, **85**, 177–184.
58. B. Shrestha and A. Vertes, Proceedings of the 60th ASMS Conference on Mass Spectrometry and Allied Topics, Vancouver, Canada, 2012.

59. R. S. Jacobson, B. Shrestha and A. Vertes, Proceedings of the 61st ASMS Conference on Mass Spectrometry and Allied Topics, Minneapolis, MN, 2013.
60. G. Agati, C. Brunetti, M. Di Ferdinando, F. Ferrini, S. Pollastri and M. Tattini, *Plant Physiol. Biochem.*, 2013, 72, 35–45.
61. M. Andersson, M. R. Groseclose, A. Y. Deutch and R. M. Caprioli, *Nat. Methods*, 2008, **5**, 101–108.
62. L. S. Eberlin, D. R. Ifa, C. Wu and R. G. Cooks, *Angew. Chem., Int. Ed.*, 2010, **49**, 873–876.
63. H. Li, B. K. Smith, B. Shrestha, L. Márk and A. Vertes, in *Mass Spectrometry Imaging of Small Molecules*, ed. L. He, Springer, Berlin, 2014, DOI: 10.1016/j.ijms.2014.06.025.

New Developments in Mass Spectrometry

Editor-in-Chief:
Professor Simon J Gaskell, *Queen Mary University of London, UK*

Series Editors:
Professor Ron M A Heeren, *FOM Institute AMOLF, The Netherlands*
Professor Robert C Murphy, *University of Colorado Denver, USA*
Professor Mitsutoshi Setou, *Hamamatsu University School of Medicine, Japan*

Titles in the Series:
1: Quantitative Proteomics
2: Ambient Ionization Mass Spectrometry

How to obtain future titles on publication:
A standing order plan is available for this series. A standing order will bring delivery of each new volume immediately on publication.

For further information please contact:
Book Sales Department, Royal Society of Chemistry, Thomas Graham House, Science Park, Milton Road, Cambridge, CB4 0WF, UK
Telephone: +44 (0)1223 420066, Fax: +44 (0)1223 420247
Email: booksales@rsc.org
Visit our website at www.rsc.org/books

Printed and bound by CPI Group (UK) Ltd, Croydon, CR0 4YY

Ambient Ionization Mass Spectrometry

Edited by

Marek Domin
Boston College, Chestnut Hill, MA, USA
Email: marek.domin@bc.edu

and

Robert Cody
JEOL USA Inc, Peabody, MA, USA
Email: cody@jeol.com

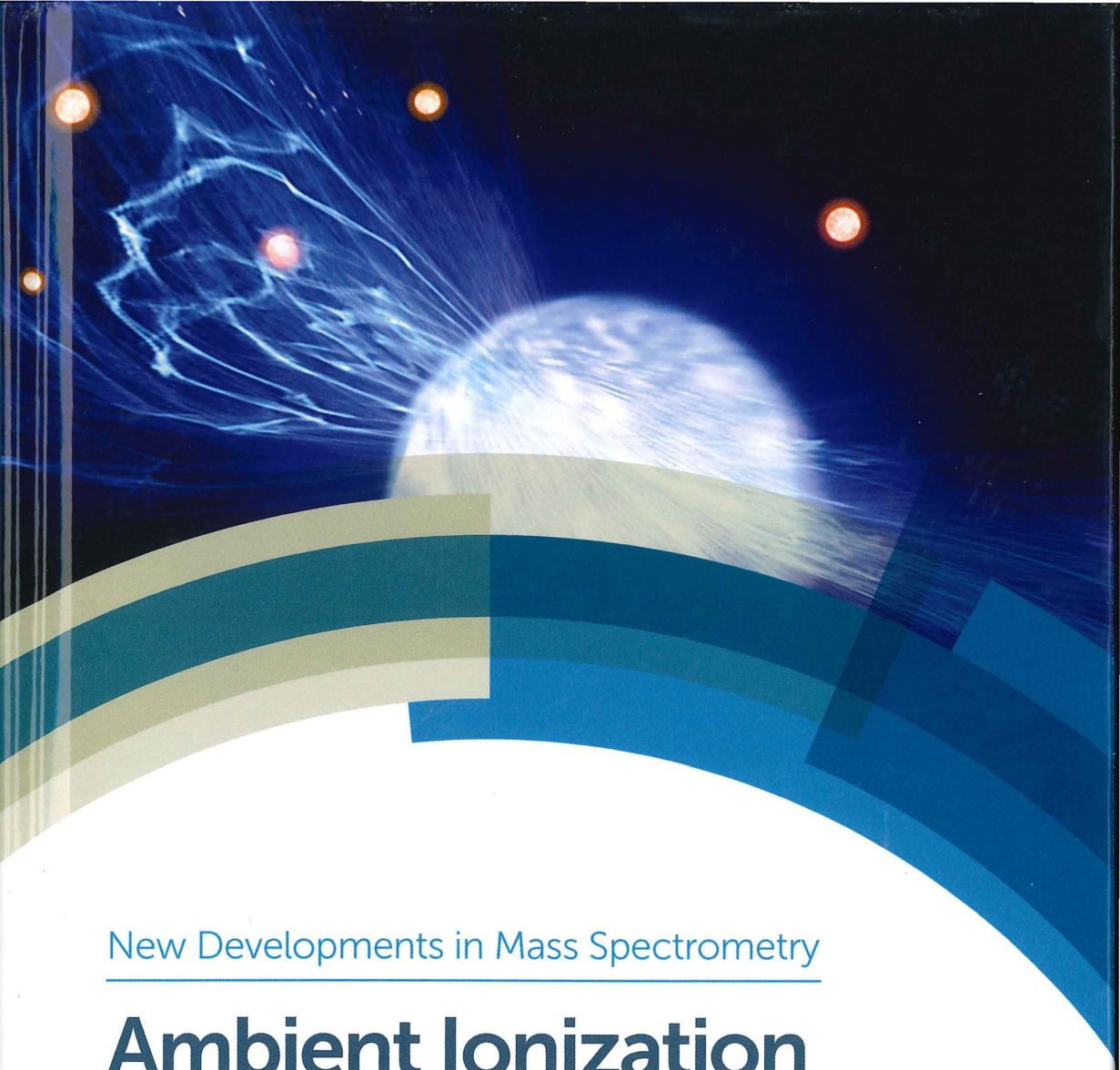

New Developments in Mass Spectrometry

Ambient Ionization Mass Spectrometry

Edited by Marek Domin and Robert Cody

ROYAL SOCIETY OF CHEMISTRY